

郭贵宾,袁晓雅,黄理金,等.土壤中典型矿物对锑的吸附-沉积行为研究[J].岩矿测试,2025,44(1):127–139. DOI: [10.15898/j.ykcs.202404210093](https://doi.org/10.15898/j.ykcs.202404210093).

GUO Guibin, YUAN Xiaoya, HUANG Lijin, et al. Adsorption-Deposition Behavior of Typical Minerals on Antimony in Soil [J]. Rock and Mineral Analysis, 2025, 44(1): 127–139. DOI: [10.15898/j.ykcs.202404210093](https://doi.org/10.15898/j.ykcs.202404210093).

## 土壤中典型矿物对锑的吸附-沉积行为研究

郭贵宾, 袁晓雅, 黄理金, 帅琴, 胡圣虹, 欧阳磊\*

(生物地质与环境地质国家重点实验室, 中国地质大学(武汉)材料与化学学院, 湖北 武汉 430074)

**摘要:** 矿物开采、煤炭燃烧等人类活动使大量的锑进入土壤, 造成严重的锑污染, 危害人类健康。厘清环境中锑的吸附-沉积行为对锑的环境归趋预测及污染防治具有重要意义, 但土壤中典型矿物对锑的吸附沉积行为缺乏系统比较, 界面吸附形态也难以表征。为了系统地比较土壤中典型矿物对锑的吸附能力差异, 本文选用土壤中常见的5种金属氧化物(赤铁矿、针铁矿、水铁矿、氧化铝、斜方锰矿)和1种黏土矿物(高岭石), 探究Sb(III)和Sb(V)在其表面的吸附热、动力学行为, 并基于原位拉曼光谱表征分析了锑的吸附形态, 推测其吸附机理。结果表明: 铁锰氧化物对锑的吸附容量较大, 而氧化铝、高岭石对锑吸附容量较小, 6种典型矿物对Sb(III)和Sb(V)吸附容量(mg/g)分别为水铁矿(101.4、55.9)>斜方锰矿(16.52、7.58)>针铁矿(13.30、5.67)>赤铁矿(5.13、3.70)>氧化铝(1.66、1.69)>高岭石(0.27、0.51); 受锑存在形态及矿物表面电位的影响, 酸性条件下有利于Sb(V)的吸附, 吸附量较之碱性环境有24%~78%增加, 而Sb(III)的吸附受pH值影响较小(变化范围0.3%~14%); 土壤中典型矿物对不同浓度的Sb(V)主要为吸附作用, 而Sb(III)在较高浓度时, 可能在矿物表面发生沉积, 形成 $Sb_2O_3$ 。本文通过采用拉曼光谱, 基于锑的特征谱峰, 可方便地对矿物表面吸附态和沉积态的锑进行原位表征。

**关键词:** 锑; 水铁矿; 斜方锰矿; 氧化铝; 吸附; 沉积; 拉曼光谱

### 要点:

- (1) 获得典型铁锰氧化物和高岭土在中性条件下对Sb(III)和Sb(V)的吸附容量、吸附动力学等参数, 并考察了pH等条件对吸附容量的影响。
- (2) 采用拉曼光谱对吸附态和沉积态Sb(III)和Sb(V)进行了原位表征, 获得Sb(III)高浓度下沉积产生的 $Sb_2O_3$ 的特征拉曼光谱信号。
- (3) 基于吸附实验数据及相关表征分析了Sb(III)和Sb(V)的吸附机制, 表明锑在本研究的矿物表面主要发生化学吸附, 高浓度Sb(III)在矿物表面可能发生沉积。

**中图分类号:** X131.3

**文献标识码:** A

锑(Sb)是一种重要的战略金属, 应用领域包括阻燃塑料、缩聚催化剂、铅酸电池、玻璃、橡胶、颜料、陶瓷、半导体等<sup>[1-2]</sup>。同时, 锑也是一种对动植物有害的非必需类金属, 其毒性、迁移性受到锑存在形式的影响<sup>[3]</sup>。环境中锑主要存在形式为 $Sb(OH)_3$ 和 $Sb(OH)_6^-$ , 其中三价锑Sb(III)的毒性明

显高于五价锑Sb(V)<sup>[4]</sup>。世界卫生组织规定饮用水中锑的最大允许浓度为20 $\mu g/L$ , 中国规定饮用水中的最大允许浓度为5 $\mu g/L$ , 锑及含锑化合物已被欧盟(EU)和美国环境保护署(USEPA)列为新兴污染物或优先关注的污染物<sup>[5]</sup>。中国锑资源丰富, 锑矿主要集中在广西、湖南、云南和贵州地区<sup>[6-7]</sup>。

收稿日期: 2024-04-21; 修回日期: 2024-07-04; 接受日期: 2024-07-11; 网络出版日期: 2024-08-07

基金项目: 国家自然科学基金项目(22106147); 湖北省自然科学基金项目(2024AFD399)

第一作者: 郭贵宾, 硕士研究生, 主要从事锑环境化学行为研究。E-mail: [3035887493@cug.edu.cn](mailto:3035887493@cug.edu.cn)。

通信作者: 欧阳磊, 博士, 副教授, 主要从事分析地球化学研究。E-mail: [ouyanglei@cug.edu.cn](mailto:ouyanglei@cug.edu.cn)。

中国也是锑资源开采大国,锑产能约占全球的78%<sup>[8]</sup>。锑矿的大量开采和冶炼,产生的尾矿废渣和矿山废石中锑含量较高。同时,有色金属冶炼、燃烧化石燃料等活动也会产生大量含锑废物,经雨水冲刷和地表径流等因素进入土壤<sup>[9]</sup>。例如某射击场和燃煤电厂附近的土壤中锑含量高达67.48mg/kg和39.29mg/kg<sup>[10-11]</sup>,造成了严重的污染。地表土壤中的锑除直接污染地表、地下水以外,还可能经由植物根部吸收富集,威胁动物和人类健康<sup>[12]</sup>。因此,厘清锑在土壤中的吸附、迁移行为对准确预测锑的环境风险具有重要意义。

进入土壤的锑可能被吸附、解吸,甚至发生氧化还原反应,自然状况下锑可以通过与金属氢氧化物发生吸附或者共沉淀形成稳定的次生锑矿物<sup>[13]</sup>,而锑矿物中的锑也可转变为溶解态,扩散至周边环境乃至地下水中。土壤中吸附锑的活性成分主要为铁、铝和锰氧化物和黏土矿物等,其中广泛存在于土壤和沉积物中的铁氧化物<sup>[14]</sup>,如针铁矿、赤铁矿和水铁矿等,对锑的固定占比可达40%~75%<sup>[15]</sup>。有研究表明,锑在铁氧化物表面的吸附、沉淀行为与矿物晶面的暴露情况及其浓度有复杂依赖关系<sup>[16]</sup>,可在氧化铁表面形成多种配位构型的内球配合物<sup>[17]</sup>,基于零价铁的锑污染土壤修复技术也有报道<sup>[18]</sup>。锰氧化物是自然界中常见的天然氧化剂,可通过氧化和吸附机制在降低锑的毒性和影响锑的迁移行为方面发挥至关重要的作用<sup>[19]</sup>,如有研究报道了天然存在的锰氧化物会降低锑的流动性和生物利用度<sup>[20]</sup>。氧化锰不同的暴露晶面对锑的吸附行为也有差异,如Sb(III)优先吸附于 $\alpha\text{-MnO}_2$ 的{310}、 $\gamma\text{-MnO}_2$ (斜方锰矿)的{131}和 $\delta\text{-MnO}_2$ 的{111}晶面<sup>[21]</sup>。铝氧化物和黏土材料虽然对锑的吸附量较低,但自然界中氧化铝和黏土矿物相对含量可能较高,对锑的影响也不可忽视<sup>[22]</sup>。研究发现Sb(V)在 $\gamma\text{-Al}_2\text{O}_3$ 可形成外配球络合物<sup>[23]</sup>,膨润土对Sb(III)和Sb(V)的最大吸附量分别为370~555 $\mu\text{g/g}$ 和270~500 $\mu\text{g/g}$ <sup>[24]</sup>。上述材料通过改性可提高对锑的吸附能力,因而可以构建锑污染的修复材料<sup>[25]</sup>。尽管目前已有文献关注天然矿物对锑的吸附、解吸行为<sup>[26-27]</sup>,但锑在天然矿物界面处形态的原位表征、其形态与锑浓度的相关性仍未见报道,了解这些基本信息将有助于深入了解锑的地球化学循环及环境风险。

因此,为探究进入土壤中不同价态锑的吸附迁移行为,有必要对土壤中典型矿物吸附锑的性能及

吸附机制进行比较与研究。本文基于土壤的主要成分及相关文献中已证实的对锑的吸附迁移行为有显著影响的组分,选择了土壤中代表性的5种金属氧化物(赤铁矿、针铁矿、水铁矿、斜方锰矿、氧化铝)和一种黏土矿物(高岭石),系统地比较了这6类矿物对Sb(III)和Sb(V)的吸附性能,获得吸附速率、吸附容量、pH值对吸附的影响等热力学、动力学参数,并结合拉曼光谱对锑在矿物表面的吸附、沉积行为进行原位表征。通过分析吸附机制,总结了上述土壤中典型矿物对锑环境迁移行为的影响,研究结果可为土壤中锑污染风险预警及阻控提供参考。

## 1 实验部分

### 1.1 材料及表征

为尽可能地反映实际土壤成分的特征,本研究除水铁矿外,其他材料均直接采用商品化的矿物材料,包括:斜方锰矿( $\gamma\text{-MnO}_2$ ,90%,上海麦克林生化科技有限公司);赤铁矿( $\alpha\text{-Fe}_2\text{O}_3$ ,99.8%,上海麦克林生化科技有限公司);针铁矿( $\text{FeHO}_2$ ,99%,上海贤鼎生物科技有限公司);氧化铝( $\alpha\text{-Al}_2\text{O}_3$ ,99.99%,艾览化工科技有限公司);高岭石( $\text{Al}_2\text{O}_3\cdot2\text{SiO}_2\cdot2\text{H}_2\text{O}$ ,分析纯,上海麦克林生化科技有限公司)。水铁矿由于稳定性较差,为保证实际存在形态的一致性,采用实验室方法合成。合成方法<sup>[28]</sup>如下:配制0.2mol/L硝酸铁(分析纯,国药集团化学试剂有限公司)溶液,在不断搅拌情况下滴加浓氨水至溶液pH=7.0,再搅拌30min。离心、超声洗涤3次,真空干燥12h。

采用X射线衍射仪(XRD,SmartLab SE,日本Rigaku公司)和比表面积测试仪(BET,ASAP2460,美国麦克仪器公司)对材料进行表征。样品处理如下:将赤铁矿、针铁矿、水铁矿、斜方锰矿、氧化铝、高岭石于真空烘箱60℃干燥12h后手动研磨后进行测试。

采用Zeta电位测试(ZEN3690,英国Malvern公司)表征材料的表面电位。样品处理如下:将材料超声分散后,采用盐酸和氢氧化钠将分散液调至不同pH值,取上清液测试样品的Zeta电位。

采用电感耦合等离子体发射光谱仪(ICP-OES,EXPEC6000,杭州谱育科技发展有限公司)测定溶液中锑浓度。仪器工作条件:功率1150W,蠕动泵转速50r/min,辅助气流速0.6L/min,雾化器气体流速0.5L/min(转子流量计测量),冲洗时间30s,积分时间15s,重复次数3次。锑元素的特征谱线为:206.8、231.1、259.8nm。

采用拉曼光谱仪 (Raman, QEPRO, 蔚海光学仪器(上海)有限公司) 对界面吸附态锑进行原位表征。测试方法及仪器条件如下: 取吸附后的矿物分散液 10 $\mu\text{L}$  滴加至玻片, 直接进行拉曼光谱测试。激光波长 780nm, 激光功率 100mW, 积分时间 10s, 积分次数 10 次, 光谱分辨率 2cm<sup>-1</sup>。拉曼测试时每个样品至少随机选取 10 个不同的位置进行光谱采集, 计算平均光谱进行后续分析。

## 1.2 Sb(III)/Sb(V) 的吸附热力学实验

将焦锑酸钾、酒石酸锑钾溶解配制成 1000mg/L 的储备溶液, 实验前按照一定比例稀释到目标浓度。进行吸附实验前, 先使用 0.1mol/L 盐酸或 0.1mol/L 氢氧化钠将 10mL 不同浓度的 Sb(III) 和 Sb(V) 初始溶液 pH 调节至 7.0, 同时加入硝酸钾控制离子强度为 10mmol/L。向溶液中加入一定量的矿物材料, 并在 25℃ 下振荡吸附 24h。取上层清液通过 0.22 $\mu\text{m}$  水系滤头过滤, 酸化, 稀释 10 倍后, 使用 ICP-OES 测定吸附后锑的浓度, 计算吸附量  $q_e(\text{mg/g})$ 。土壤铁锰氧化物和黏土矿物的用量分别为: 赤铁矿 10mg、针铁矿 10mg、水铁矿 5mg、氧化铝 20mg、斜方锰矿 10mg、高岭石 50mg。实验中每组样品均平行测定 3 次, 取平均值进行分析。

## 1.3 Sb(III)/Sb(V) 的吸附动力学实验

取 30mL 浓度为 15mg/L 的 Sb(III) 和 Sb(V) 溶

液, pH 调节至 7.0, 加入硝酸钾保持离子强度为 10mmol/L。加入一定量矿物后于 25℃ 下振荡吸附, 在吸附不同时间后, 取上层清液通过 0.22 $\mu\text{m}$  水系滤头过滤, 酸化、稀释, ICP-OES 检测。土壤铁锰氧化物和黏土矿物的用量分别为: 赤铁矿 60mg、针铁矿 30mg、水铁矿 7.5mg、氧化铝 150mg、斜方锰矿 30mg、高岭石 600mg。实验中每组样品均平行测定 3 次, 取平均值进行分析。

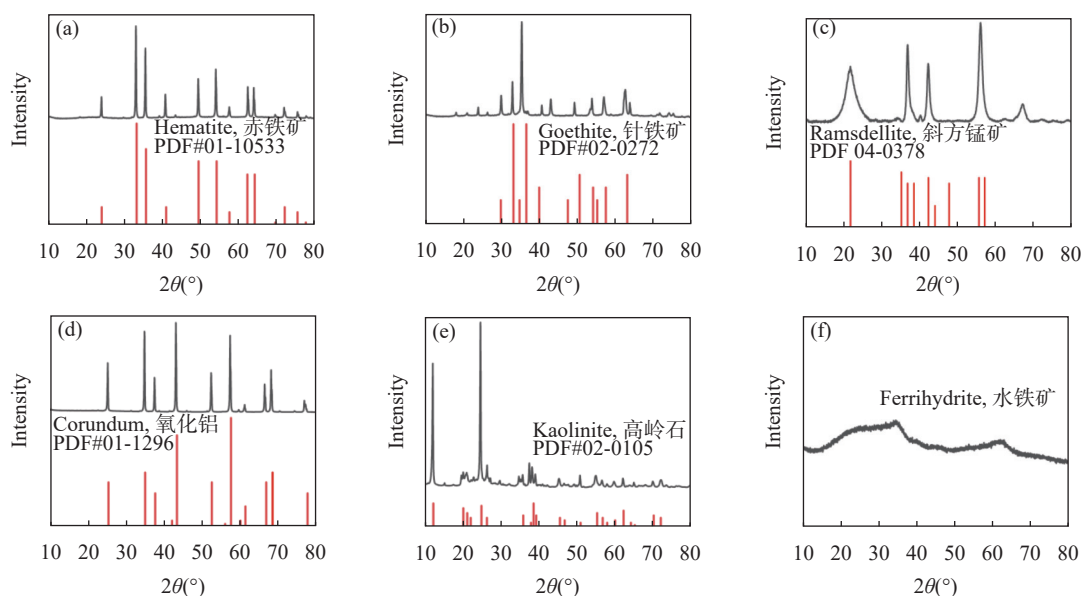
## 1.4 pH 值对 Sb(III)/Sb(V) 吸附的影响实验

分别将 30mL 浓度为 15mg/L 的 Sb(III) 和 Sb(V) 溶液的初始溶液 pH 调节为 4.0、7.0、9.0, 加入硝酸钾保持离子强度为 10mmol/L。加入一定量矿物材料后, 于 25℃ 下振荡吸附。吸附 24h 后, 取上层清液通过 0.22 $\mu\text{m}$  水系滤头过滤, 酸化、稀释, ICP-OES 检测。矿物用量同 1.2 节。实验中每组样品均平行测定 3 次, 计算平均值进行分析。

## 2 结果与讨论

### 2.1 六种矿物材料表征

为了解矿物的晶型及物相类型, 采用 X 射线衍射谱分析矿物, 其谱图见图 1。6 种矿物的 XRD 谱图与标准卡片对照, 除水铁矿无明显晶型以外, 另外 5 种矿物的 XRD 谱图与矿物标准谱图吻合较好, 且无其他杂相; 水铁矿为无定型矿物, 其 XRD 谱图与文献报道结果<sup>[29]</sup>一致。矿物的比表面积采用



a—赤铁矿; b—针铁矿; c—斜方锰矿; d—氧化铝; e—高岭石; f—水铁矿。

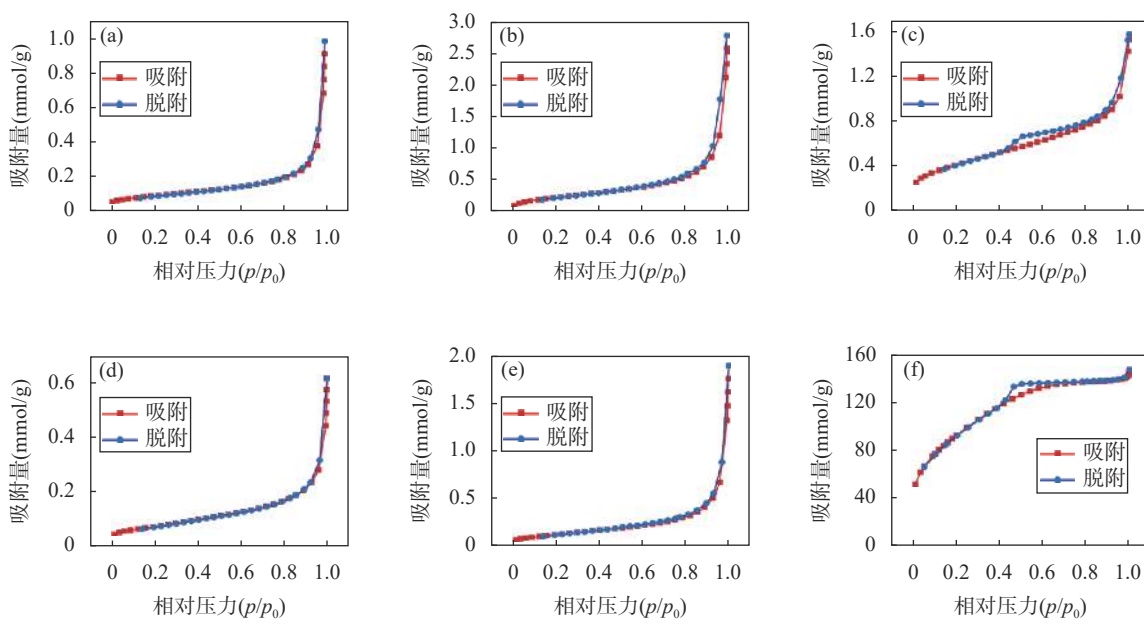
图1 六种矿物材料的 X 射线衍射谱图

Fig. 1 The XRD patterns of the six minerals.

Brunauer-Emmett-Teller法(BET)进行测定,分别测定了6种材料的氮气吸脱附曲线,结果如图2所示。经计算,6种矿物材料赤铁矿、针铁矿、斜方锰矿、氧化铝、高岭石和水铁矿的比表面积分别为6.6、18.9、32.3、6.1、10.5、 $335.6\text{m}^2/\text{g}$ 。其中,赤铁矿、针铁矿、斜方锰矿、氧化铝、高岭石的氮气吸附-解吸等温线符合IV型吸附等温线,说明这5种材料具有介孔结构(孔直径为2~50nm);水铁矿的氮气吸附-解吸等温线符合I型吸附等温线,说明水铁矿具有微孔结构(孔直径<2nm)。

## 2.2 六种矿物材料对锑的吸附动力学研究

中性条件下6种矿物材料对Sb(III)/Sb(V)的吸附动力学如图3所示,吸附数据拟合均更符合准二级动力学模型(表1),表明化学吸附是主要的速率控制步骤。Sb(III)和Sb(V)在吸附初始阶段即前2h内吸附速率较快;随着吸附时间进一步延长,矿物表面的活性吸附位点逐渐饱和,吸附速率在2~6h内逐渐下降;除斜方锰矿吸附Sb(III)外,其他材料均在24h左右达到吸附平衡。斜方锰矿吸附Sb(III)在吸附初期(约5min)迅速达到较高的吸附量,该过程



a—赤铁矿; b—针铁矿; c—斜方锰矿; d—氧化铝; e—高岭石; f—水铁矿。

图2 六种矿物材料的氮气吸附-脱附等温线

Fig. 2 The  $\text{N}_2$  adsorption-desorption isotherms of the six minerals.

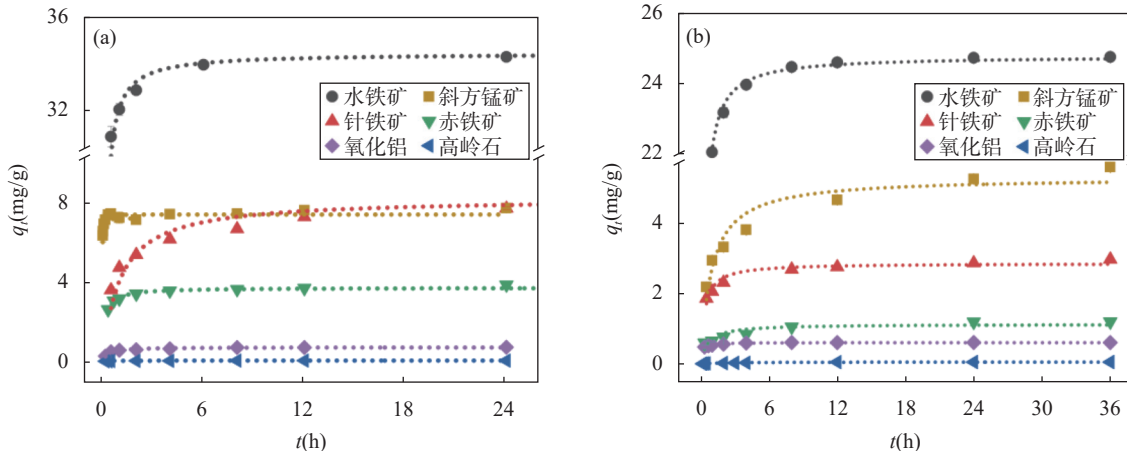


图3 六种矿物材料吸附(a) Sb(III) 和(b) Sb(V) 的吸附动力学

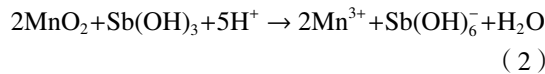
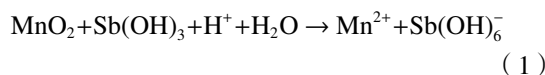
Fig. 3 The adsorption kinetics of (a) Sb(III) and (b) Sb(V) on the six minerals.

表1 Sb(III)和Sb(V)的吸附动力学拟合参数

Table 1 Fitting parameters of adsorption kinetics for Sb(III) and Sb(V).

矿物材料	Sb(III)准一级动力学			Sb(III)准二级动力学			Sb(V)准一级动力学			Sb(V)准二级动力学		
	$K_1$ ( $\text{h}^{-1}$ )	$q_e$ (mg/g)	$R^2$	$K_2$ [g/(mg·h)]	$q_e$ (mg/g)	$R^2$	$K_1$ ( $\text{h}^{-1}$ )	$q_e$ (mg/g)	$R^2$	$K_2$ [g/(mg·h)]	$q_e$ (mg/g)	$R^2$
赤铁矿	2.58	7.35	0.750	0.88	7.45	0.911	1.15	1.05	0.721	1.52	1.13	0.913
针铁矿	0.53	7.83	0.896	0.12	8.22	0.986	1.75	2.74	0.721	1.05	2.86	0.924
水铁矿	4.74	33.7	0.645	0.40	34.4	0.957	3.33	24.1	0.946	0.33	24.8	0.999
斜方锰矿	82.1	7.03	0.716	41.9	7.22	0.940	0.75	4.90	0.832	0.20	5.30	0.921
氧化铝	6.58	0.71	0.958	15.5	0.73	0.976	4.49	0.59	0.631	16.1	0.61	0.933
高岭石	6.45	0.08	0.927	132.8	0.08	0.973	0.34	0.09	0.894	9.17	0.06	0.939

可能与其对 Sb(III) 的氧化作用有关, 反应方程式如以下 (1) 和 (2) 所示, 氧化反应<sup>[30]</sup> 以及生成 Sb(V) 的吸附共同作用导致前期吸附速率较快<sup>[31]</sup>; 在斜方锰矿氧化 Sb(III) 的过程中, 可能破坏其表面结构, 导致少部分吸附态锑的溶出<sup>[25]</sup>, 因此 20min 后 Sb(III) 的吸附量有一定程度地下降。随吸附时间的继续延长, Sb(III) 的吸附逐步达到平衡。



### 2.3 六种矿物对锑的吸附等温线

为了比较 6 种矿物材料对锑的吸附能力, 分别测得中性条件下 Sb(III)/Sb(V) 在 6 种矿物表面吸附的吸附等温线, 结果如图 4 所示, 随着 Sb(III)/Sb(V) 初始浓度的增加, 矿物对锑的吸附量增加。分别采用 Langmuir 和 Freundlich 等温线模型对吸附等温线进行了拟合, 相关拟合参数列于表 2。结果表明,

Freundlich 模型拟合结果的  $R^2$  值均大于 Langmuir 模型, 表明锑在上述 6 种矿物表面主要发生多层吸附。Freundlich 系数 ( $K_F$ ) 反映了吸附质在吸附剂表面的吸附程度,  $K_F$  越高, 表示吸附越有效, 因此对于矿物吸附锑而言, 铁氧化物和锰氧化物对锑的  $K_F$  较大, 表明上述材料与锑的亲和性较强<sup>[32]</sup>。

6 种矿物对不同价态锑的吸附能力不同, 整体而言, 同种矿物材料对 Sb(III) 的吸附容量大于该矿物对 Sb(V) 的吸附容量, 表明进入土壤的 Sb(III) 相较于 Sb(V) 更容易被土壤矿物吸附固定。对比吸附容量, 单位质量土壤矿物对 Sb(III) 和 Sb(V) 的最大吸附容量 (mg/g) 分别为: 水铁矿 (101.4、55.9)> 斜方锰矿 (16.52、7.58)> 针铁矿 (13.30、5.67)> 赤铁矿 (5.13、3.70)> 氧化铝 (1.66、1.69)> 高岭石 (0.27、0.51)。土壤中的铁氧化物一般具有较大的比表面积、高孔隙率和表面电荷高等特点, 而且对锑有较强的化学亲和力, 因此是控制锑元素迁移和生物利用度的关键成分<sup>[33]</sup>。相比于晶型的针铁矿和赤铁矿, 水铁矿的比表面积更大, 吸附活性位点更多, 因此对

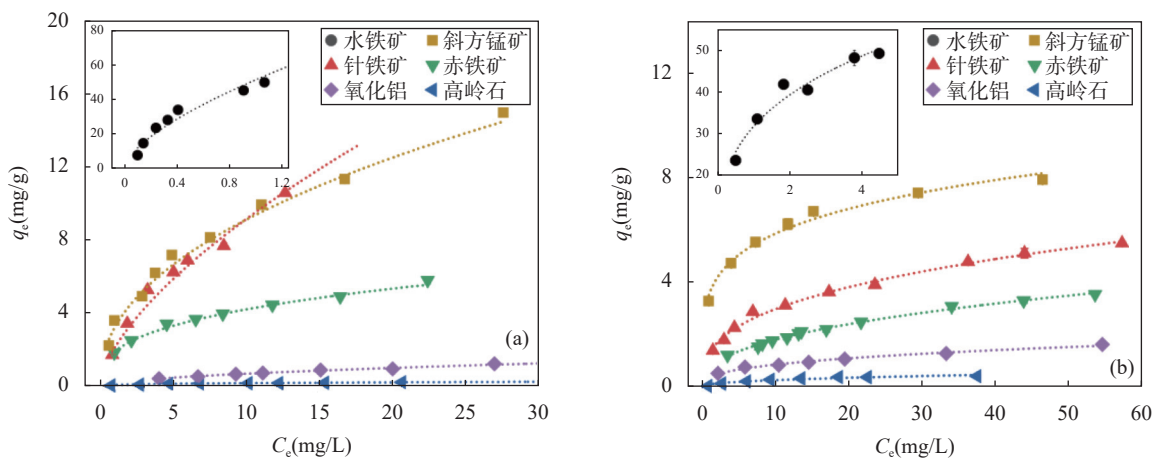


图4 六种矿物材料吸附(a) Sb(III)和(b) Sb(V)的吸附等温线

Fig. 4 Adsorption isotherms of (a) Sb(III) and (b) Sb(V) on the six minerals.

表2 Sb(III)和Sb(V)的吸附等温线拟合参数

Table 2 Fitting parameters of adsorption isotherms of Sb(III) and Sb(V).

材料	Sb(III)-Langmuir			Sb(III)-Freundlich			Sb(V)-Langmuir			Sb(V)-Freundlich		
	$K_L$ (L/mg)	$q_m$ (mg/g)	$R^2$	$n$	$K_F$ [(mg/g)(mg/L) $^{-1/n}$ ]	$R^2$	$K_L$ (L/mg)	$q_m$ (mg/g)	$R^2$	$n$	$K_F$ [(mg/g)(mg/L) $^{-1/n}$ ]	$R^2$
赤铁矿	0.48	5.13	0.961	2.90	1.90	0.996	0.11	3.70	0.925	2.43	0.70	0.997
针铁矿	0.21	13.30	0.834	2.22	3.05	0.997	0.14	5.67	0.987	2.79	1.30	0.994
水铁矿	1.01	101.4	0.980	2.09	45.3	0.979	1.00	55.9	0.789	4.62	31.7	0.987
斜方锰矿	0.15	16.52	0.964	2.19	3.19	0.993	0.76	7.58	0.950	4.62	3.56	0.995
氧化铝	0.08	1.66	0.961	1.84	0.20	0.993	0.10	1.69	0.871	2.75	0.36	0.983
高岭石	0.21	0.27	0.967	2.96	0.08	0.957	0.12	0.51	0.990	2.27	0.09	0.921

锑的吸附能力更强<sup>[34]</sup>。土壤中锰氧化物尽管含量较低,但由于锰具有丰富的价态和较强的氧化能力,因此可介导锑等变价金属发生氧化还原反应<sup>[21]</sup>。此外,锰氧化物对锑的亲和作用也会参与锑的吸附固定,因此锰氧化物在控制锑的迁移和形态转化行为方面发挥着重要的作用。斜方锰矿对Sb(III)的吸附量大于Sb(V),说明在介导Sb(III)的氧化过程中,斜方锰矿自身的晶体结构可能发生改变,从而提供更多的活性位点,使得Sb(III)的吸附量提高<sup>[21]</sup>。氧化铝和黏土矿物高岭石对锑的吸附量较低,原因是这类矿物对锑的化学亲和性较弱<sup>[22]</sup>,同时比表面积也较小。但由于某些土壤中,如岩石矿床风化沉积土壤、河流沉积土壤,氧化铝和高岭石的含量可能远高于铁氧化物或锰氧化物,因此对于这类情况,上述矿物对土壤中锑迁移行为的影响也不容忽视。

#### 2.4 pH值对六种矿物材料吸附Sb(III)/Sb(V)行为的影响

为了探究可能的吸附机制,对pH值对矿物材料吸附锑性能的影响进行了实验,结果如图5所示。6种矿物材料对Sb(III)的吸附在实验的pH条件下吸附量变化不大(0.3%~14%),而随着pH值的升高,6种矿物材料对Sb(V)的吸附量均有所下降(24%~

78%),表明偏碱性不利于Sb(V)的吸附。相较Sb(III)而言,Sb(V)的吸附量下降程度更大。矿物材料的Zeta电位表征结果(图5c)显示,赤铁矿、针铁矿、水铁矿、斜方锰矿、氧化铝、高岭石的等电点分别为3.1、4.4、7.2、4.5、7.8和1.6;根据锑在水溶液中的形态分布曲线,实验条件下Sb(III)、Sb(V)主要存在形态分别为Sb(OH)<sub>3</sub>和Sb(OH)<sub>6</sub><sup>-</sup>。由于Sb(III)主要以分子形式存在,因此受静电吸附作用的影响较小,说明矿物对Sb(III)的吸附主要依靠化学吸附等机制;对于Sb(V),尽管静电吸附作用有一定的贡献,例如酸性条件下,水铁矿、针铁矿、斜方锰矿、氧化铝带正电荷,有利于带负电的Sb(V)的吸附,但整体而言,静电吸附的贡献有限,矿物对Sb(V)的吸附主要通过化学吸附等形式完成。类似的现象也在砷、镉等重金属的吸附中观测到<sup>[35-36]</sup>。由于高岭石在研究的pH范围内均带负电荷,不利于Sb(V)的吸附,这与观测到的低吸附量一致。

#### 2.5 Sb(III)/Sb(V)在矿物表面吸附沉积后拉曼检测

有文献报道,当平衡浓度较低时,土壤矿物对锑吸附主要通过表面化学吸附,而随着表面浓度的增加,超过饱和浓度后,锑可能在矿物表面发生沉积现象<sup>[37]</sup>。为了验证上述现象,采集了更高平衡浓度

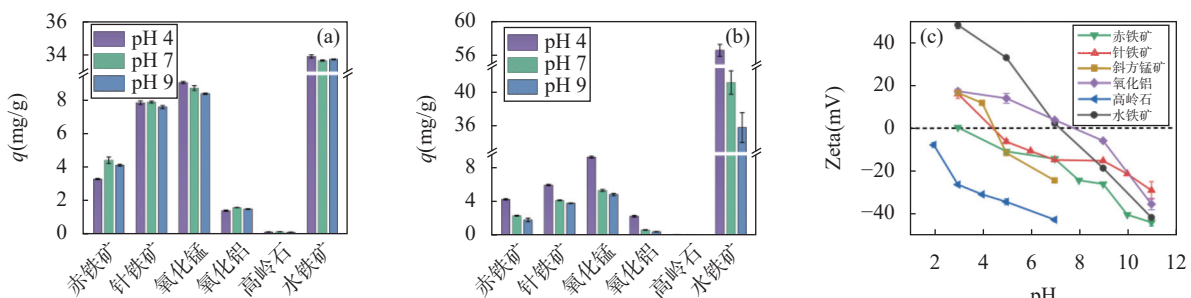


图5 pH值对(a)Sb(III)、(b)Sb(V)吸附的影响和(c)六种矿物的Zeta电位

Fig. 5 Effect of pH on the adsorption of (a) Sb(III), (b) Sb(V) on the minerals and (c) the Zeta potential of the six minerals.

下锑的吸附等温线,结果如图6所示。结果表明,随着平衡浓度的进一步增大,矿物对锑的吸附容量会进一步增大;吸附等温线拟合数据表明,锑在矿物表面吸附符合Freundlich多层吸附模型;特别是对于Sb(III)吸附于针铁矿和赤铁矿表面,还观测到吸附量激增的现象,推测发生了表面沉积现象。

由于Sb(III)沉积后可能以 $Sb_2O_3$ 形式存在,拉曼光谱是一种分子指纹光谱,不仅对矿物材料的结构敏感,同时锑的氧化物也有特征拉曼谱峰,非常适合于这类表面沉积现象的原位表征,因此本实验采用拉曼光谱对吸附锑后的矿物进行表征,结果如图7和图8所示。可见除水铁矿外,其他5种矿物

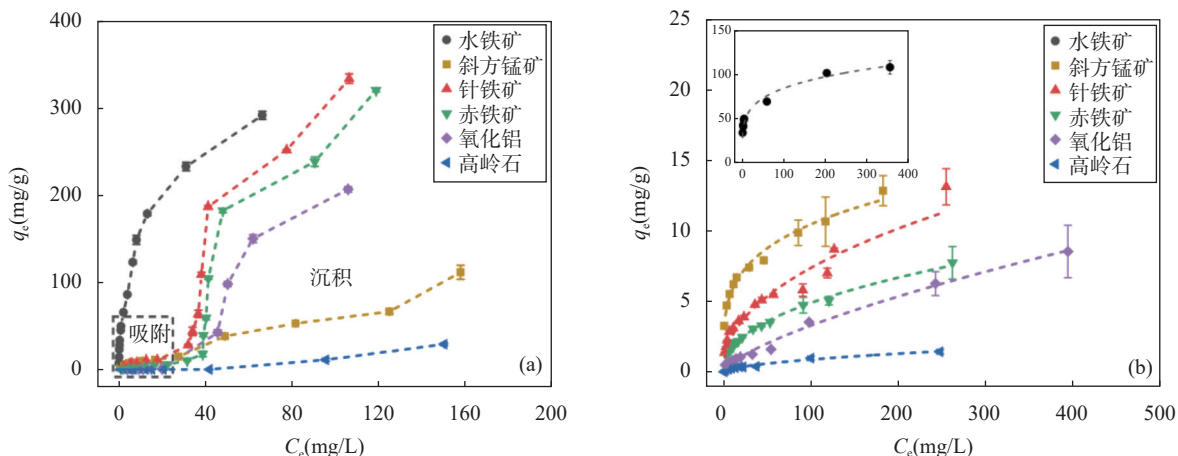
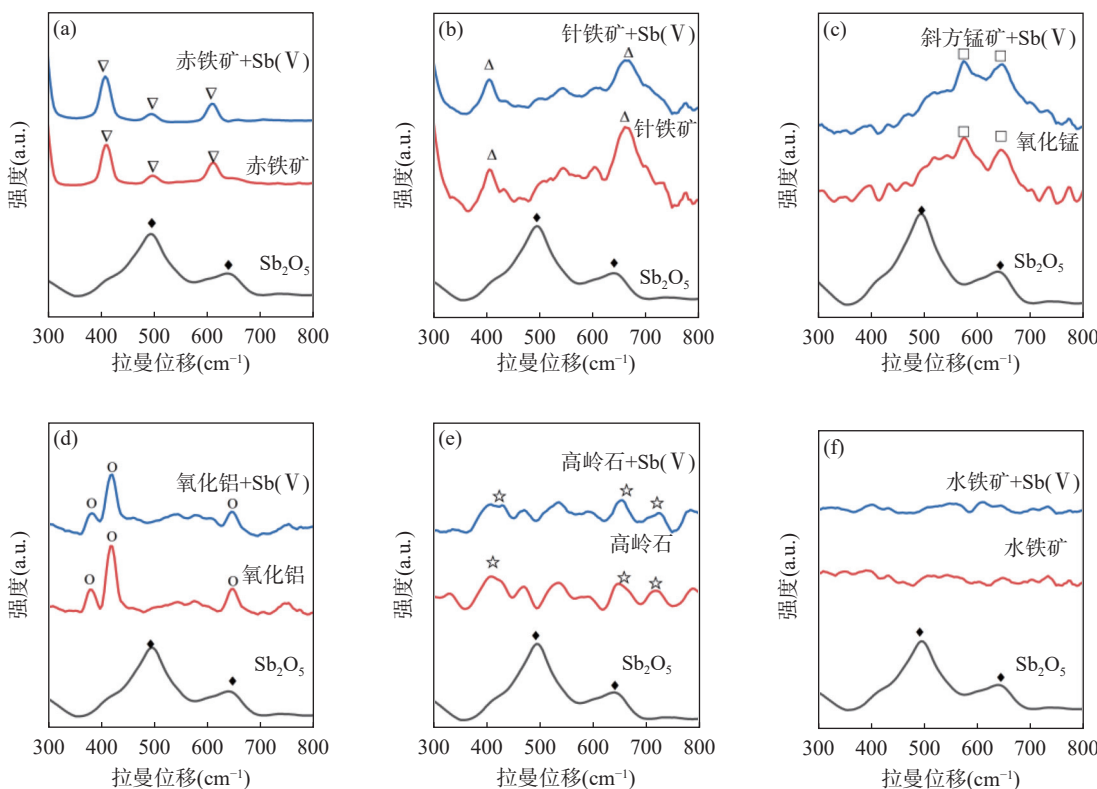


图6 高浓度(a) Sb(III) 和(b) Sb(V) 在6种矿物上的吸附等温线

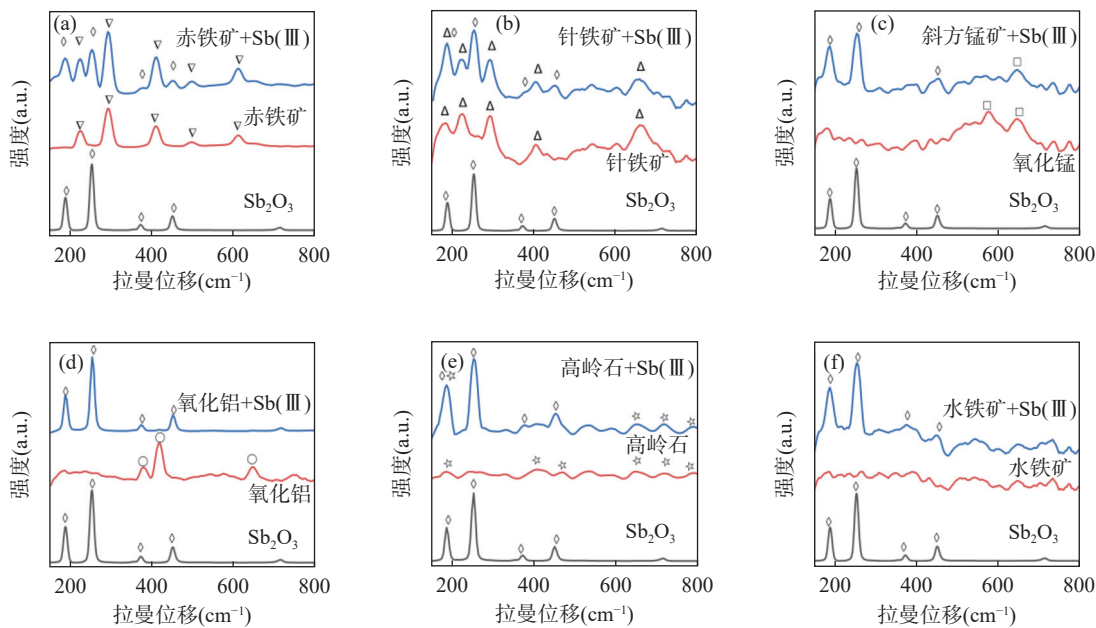
Fig. 6 Adsorption isotherms of high concentrations of (a) Sb(III) and (b) Sb(V) on the six minerals.



a—赤铁矿; b—针铁矿; c—斜方锰矿; d—氧化铝; e—高岭石; f—水铁矿。

图7 六种矿物材料吸附Sb(V)前后的拉曼光谱图

Fig. 7 Raman spectra of the six minerals before and after Sb(V) adsorption.



a—赤铁矿；b—针铁矿；c—斜方锰矿；d—氧化铝；e—高岭石；f—水铁矿。

图8 六种矿物材料吸附 Sb(III) 前后的拉曼光谱谱图

Fig. 8 Raman spectra of the six minerals before and after Sb(III) adsorption.

具有明显的特征峰。结合已有相关文献报道,对获得的特征拉曼峰的归属进行了归纳,相应的峰位及归属列于表3。对于高浓度的Sb(V)吸附后的矿物材料,并没有获得Sb(V)氧化物 $\text{Sb}_2\text{O}_5$ 的特征峰,表明并没有明显的沉积现象出现,主要以吸附作用为主;而对于Sb(III),如图8所示,出现了明显的 $\text{Sb}_2\text{O}_3$ 特征峰。位于 $190\text{cm}^{-1}$ 和 $452\text{cm}^{-1}$ 的拉曼峰可归属于Sb—O—Sb间的弯曲振动,而 $256$ 、 $357$ 、 $374$ 和 $715\text{cm}^{-1}$ 的拉曼峰则可归属于Sb—O—Sb间的伸缩振动<sup>[38]</sup>。上述特征峰与矿物立方晶型 $\alpha$ - $\text{Sb}_2\text{O}_3$ 的

特征谱峰一致,表明表面沉积主要形成 $\alpha$ 型 $\text{Sb}_2\text{O}_3$ 。上述结果证实,高浓度条件下,Sb(III)可能在矿物材料发生沉积现象,生成 $\alpha$ 型 $\text{Sb}_2\text{O}_3$ ,与化学吸附态Sb(III)相比,这类Sb可能具有更高的环境迁移性,因此具有更高的环境风险,值得关注。

从上述结果可见,拉曼光谱可以较为简便地对Sb(III)的沉积行为进行原位表征。但拉曼光谱的检测灵敏度较低,因此对于浓度较低的吸附态的Sb(V)和Sb(III),难以直接检测,结合表面增强拉曼光谱等技术,有望提高检测的灵敏度。

表3 Sb(III)或Sb(V)氧化物和相关矿物的拉曼光谱特征峰位及归属

Table 3 The characteristic Raman peaks of Sb(III) or Sb(V) oxides and the minerals and their assignment.

材料	特征峰 ( $\text{cm}^{-1}$ )	归属	材料	特征峰 ( $\text{cm}^{-1}$ )	归属
$\text{Sb}_2\text{O}_3$ <sup>[38-39]</sup>	190	$\text{F}_{2g}$ 振动	针铁矿 <sup>[40-41]</sup>	224	$\text{Fe}-\text{O}$ 拉伸振动
	374	$\text{F}_{2g}$ 振动		405	$\text{Fe}-\text{OH}$ 拉伸振动
	452	$\text{A}_g$ 振动		666	$\text{Fe}-\text{O}$ 拉伸振动
$\text{Sb}_2\text{O}_5$ <sup>[42-43]</sup>	495	Sb-O 伸缩振动	斜方锰矿 <sup>[44-45]</sup>	575	$\text{Mn}-\text{O}$ 拉伸振动
	635	Sb-O 伸缩振动		645	$\text{Mn}-\text{O}$ 对称伸缩振动
赤铁矿 <sup>[46-47]</sup>	227	$\text{A}_{1g}$ 振动	高岭石 <sup>[48-49]</sup>	189	$\text{A}_{1g}(\nu_1)\text{AlO}_6$ 振动
	293	$\text{E}_g$ 振动		409	$\nu_2(\text{e})\text{SiO}_4$ 振动
	413	$\text{E}_g$ 振动		460	$\nu_2(\text{e})\text{SiO}_4$ 振动
	499	$\text{E}_g$ 振动		640	$\text{Si}-\text{O}-\text{Al}$ 伸缩振动
	614	$\text{E}_g$ 振动		717	$\text{Si}-\text{O}-\text{Al}$ 伸缩振动
氧化铝 <sup>[50-51]</sup>	378	$\text{E}_g$ 振动		787	OH 伸缩振动
	417	$\text{A}_{1g}$ 振动			

### 3 结论

选取6种土壤中典型矿物(赤铁矿、针铁矿、水铁矿、氧化铝、斜方锰矿和高岭石),研究了Sb(Ⅲ)和Sb(V)在上述矿物表面的吸附热、动力学行为,并采用拉曼光谱对吸附界面的锑进行了原位表征。研究结果表明,选取的矿物对锑的吸附量有以下顺序:水铁矿>斜方锰矿>针铁矿>赤铁矿>氧化铝>高岭石;铁氧化物对锑有较强的吸附性,其中水铁矿由于其较大的比表面积,吸附贡献较大;斜方锰矿由于具有较强的氧化能力,可通过氧化作用氧化Sb(Ⅲ),该过程中矿物结构可能发生改变,从而进一步增强对锑的吸附能力;氧化铝和高岭石由于与锑的亲和力较弱,对锑的吸附贡献较小。pH影响实验

证实,静电吸附作用对Sb(V)的吸附有一定的贡献,但整体而言Sb(V)和Sb(Ⅲ)主要依靠化学吸附在矿物表面进行吸附。高浓度吸附等温线实验和拉曼光谱表征结果证实,在较高平衡浓度下,Sb(V)主要发生化学吸附,而Sb(Ⅲ)可能在矿物表面发生沉积,生成 $\alpha$ 型Sb<sub>2</sub>O<sub>3</sub>,从而产生与化学吸附态Sb(Ⅲ)不同的环境迁移行为。

拉曼光谱可方便地用于矿物表面吸附态和沉积态锑的原位光谱表征。但实际土壤中各矿物组分的含量可能有显著差异,要准确评价锑在实际土壤中的吸附、迁移行为,还需要系统地表征各组分的含量、粒度信息,同时结合实际土壤的理化条件(如pH、离子强度、水分和有机质等),综合分析锑的环境行为。

## Adsorption-Deposition Behavior of Typical Minerals on Antimony in Soil

GUO Guibin, YUAN Xiaoya, HUANG Lijin, SHUAI Qin, HU Shenghong, OUYANG Lei\*

(State Key Laboratory of Biogeology and Environmental Geology, Faculty of Materials Science and Chemistry, China University of Geosciences (Wuhan), Wuhan 430074, China)

### HIGHLIGHTS

- (1) Parameters such as the adsorption capacity and adsorption kinetics of Sb(Ⅲ) and Sb(V) by typical iron-manganese oxides and kaolinite under neutral conditions were obtained, and the effects of pH and other conditions on the adsorption capacity were investigated.
- (2) The *in situ* characterization of adsorbed and deposited Sb(Ⅲ) and Sb(V) was conducted using Raman spectroscopy, and the characteristic Raman spectral signals of Sb<sub>2</sub>O<sub>3</sub> formed by deposition at high concentrations of Sb(Ⅲ) were obtained.
- (3) Based on the adsorption experimental data and related characterizations, the adsorption mechanisms of Sb(Ⅲ) and Sb(V) were analyzed. The results showed that chemical adsorption was the primary mechanism for antimony on the surface of the studied minerals, and deposition of high concentrations of Sb(Ⅲ) on the mineral surface was also possible.

**ABSTRACT:** Human activities such as mineral mining and coal combustion cause a large amount of antimony to enter into environmental soil. Exploring the adsorption deposition behavior of antimony on typical soil minerals is important for predicting the environmental fate of antimony and preventing its pollution. Thus, six kinds of commonly found metal hydroxides and clay minerals in soil (namely hematite, goethite, ferrihydrite, aluminum oxide, ramsdellite, and kaolinite) were selected to investigate the adsorption thermodynamic and kinetic behavior of Sb(Ⅲ) and Sb(V) on their surfaces, and speculate the adsorption mechanism. The order of adsorption capacities (mg/g) of six soil minerals for Sb(Ⅲ)/Sb(V) were as follows: ferrihydrite (101.4, 55.9)>ramsdelite (16.52, 7.58)>goethite (13.30, 5.67)>hematite (5.13, 3.70)>aluminum oxide (1.66, 1.69)>kaolinite (0.27, 0.51). Affected by the speciation of antimony and the surface potential of minerals, acidic conditions were favorable for the adsorption of Sb(V), while the adsorption of Sb(Ⅲ) was less affected by pH. The Sb<sub>2</sub>O<sub>3</sub> formed after deposition was

characterized *in situ* by Raman spectroscopy. Sb(V) adsorbed on the mineral by adsorption at different concentrations, while Sb(III) deposits on the mineral surface at higher concentrations. The BRIEF REPORT is available for this paper at <http://www.ykcs.ac.cn/en/article/doi/10.15898/j.ykcs.202404210093>.

**KEY WORDS:** antimony; ferrihydrite; ramsdellite; aluminum oxide; adsorption; sedimentation; Raman spectroscopy

## BRIEF REPORT

**Significance:** Antimony (Sb) is a non-essential metal, primarily introduced into the environment through anthropogenic activities, such as mineral extraction. It can enter the human body through respiratory tract, skin contact, and food chain, causing antimony poisoning. In soil, it may undergo adsorption, desorption, or redox reactions. Under natural conditions, it can form stable secondary minerals through adsorption or co-precipitation with metal hydroxides. Conversely, antimony present in these minerals may also dissolve and diffuse into the surrounding environment, including groundwater, contributing to environmental contamination. Exploring the adsorption deposition behavior of typical soil minerals on antimony is of great significance for predicting its environmental fate and preventing pollution.

The active components that adsorb antimony in soil are mainly iron, aluminum, manganese oxides, and clay minerals. The fixed proportion of antimony in soil iron oxides such as goethite, hematite, and ferrihydrite can reach 40% to 75%<sup>[15]</sup>. Studies have shown that the adsorption and precipitation behavior of antimony on the surface of iron oxides have a complex dependence on the exposure and concentration of mineral crystal planes<sup>[16]</sup>, and can form various coordination configurations of inner sphere complexes on the surface of iron oxides<sup>[17]</sup>. Research has indicated that manganese oxide plays a vital role in mitigating the toxicity of antimony and influencing its migration behavior via oxidation and adsorption mechanisms.<sup>[19]</sup> The adsorption behavior of antimony varies on different exposed crystal faces of manganese oxide, such as Sb(III) preferentially adsorbing on the {310} crystal face of  $\alpha\text{-MnO}_2$ , {131} crystal face of  $\gamma\text{-MnO}_2$  (ramsdellite), and {111} crystal face of  $\delta\text{-MnO}_2$ <sup>[21]</sup>. Although aluminum oxide and clay materials have lower adsorption capacity for antimony, their relative contents may be higher, and their impact on cannot be ignored<sup>[22]</sup>. Research has found that Sb(V) can form exosphere complexes on  $\gamma\text{-Al}_2\text{O}_3$ <sup>[23]</sup>, and the maximum adsorption capacities of bentonite for Sb(III) and Sb(V) are 370–555 $\mu\text{g/g}$  and 270–500 $\mu\text{g/g}$ , respectively<sup>[24]</sup>. Although existing literature has focused on the adsorption and desorption behavior of natural minerals towards antimony<sup>[26–27]</sup>, there have been no reports on the *in situ* characterization of antimony morphology at natural mineral interfaces and its correlation with antimony concentration.

In this study, the adsorption performance and mechanism of antimony on six selected oxides and minerals were determined. Generally, the adsorption of Sb(V) and Sb(III) was predominantly governed by chemisorption, with electrostatic adsorption also playing a notable role in the adsorption of Sb(V). Results from high-concentration adsorption isotherm experiments and Raman spectroscopic analysis confirmed that at elevated equilibrium concentrations, Sb(V) primarily undergoes chemisorption, whereas Sb(III) tends to deposit on the oxide and mineral surfaces to form  $\alpha\text{-Sb}_2\text{O}_3$ . This deposition behavior may result in distinct environmental mobility for Sb(III) compared to its chemisorbed state. These findings provide valuable insights for the risk assessment and management of antimony contamination in soils.

**Methods:** Hematite, ramsdellite, kaolinite, goethite and aluminum oxide were purchased from a reagent company, while ferrihydrite was prepared as follows<sup>[28]</sup>: concentrated ammonia solution was added to 0.2mol/L  $\text{Fe}(\text{NO}_3)_3$  solution dropwise under stirring, until the solution pH reached 7.0. After further reaction for 30min, the product was centrifuged, ultrasonically washed 3 times, and vacuum dried.

**(1) Adsorption experiments.** The initial pH of 10mL of Sb(III) and Sb(V) solutions were adjusted to 7.0 using 0.1mol/L hydrochloric acid or 0.1mol/L sodium hydroxide, and potassium nitrate was added to control the ion strength to 10mmol/L. A predetermined amount of minerals were added to the solution and oscillated for adsorption at 25°C for 24h. The upper clear liquid was removed and ICP-OES used to detect the concentration of antimony. The adsorption amount  $q_e$ (mg/g) was then calculated. During the experiment, each group of samples was performed in triplicate and the average value was taken for analysis.

**(2) Raman experiment.** Mineral dispersion (10μL) after adsorption was dropped onto a glass slide for Raman testing. The following parameters were used: laser wavelength of 780nm, laser power of 100mW, integration time of 10s, integration times of 10, and a spectral resolution of 2cm<sup>-1</sup>.

**Data and Results:** The XRD spectra of 6 minerals were compared with the standard card. Except for ferrihydrite, which had no obvious crystal structure, the XRD spectra of the other 5 minerals were in good agreement with the mineral standard spectra, and there were no other impurities (Fig.1). Ferrihydrite is an amorphous mineral, and its XRD spectrum is consistent with the results reported in the literature<sup>[29]</sup>. The specific surface areas of hematite, goethite, ramsdellite, alumina oxide, kaolinite, and ferrihydrite (Fig.2) were 6.6, 18.9, 32.3, 6.1, 10.5, and 335.6m<sup>2</sup>/g, respectively. The adsorption rates of Sb(III) and Sb(V) were relatively fast within the first 2h. As the adsorption time increased, the active adsorption sites on the mineral surface gradually became saturated, and the adsorption rate gradually decreased within 2–6h. Except for the adsorption of Sb(III) by ramsdellite, all other materials reached adsorption equilibrium around 24h (Fig.3). The adsorption of Sb(III) by ramsdellite rapidly reached a high adsorption capacity in the initial stage (about 5min). The adsorption capacity of the same mineral material for Sb(III) was greater than that for Sb(V). The order of adsorption capacities (mg/g) of six soil minerals for Sb(III)/Sb(V) were as follows: ferrihydrite (101.4, 55.9)>ramsdelite (16.52, 7.58)>goethite (13.30, 5.67)>hematite (5.13, 3.70)>aluminum oxide (1.66, 1.69)>kaolinite (0.27, 0.51) (Fig.4). The adsorption capacities of mineral materials for Sb(III) did not change significantly (0.3%–14%) under different pH conditions, while with the increase of pH value, the adsorption capacity of mineral materials for Sb(V) decreased (24%–78%) (Fig.5). After exceeding the saturation concentration, Sb(III) deposited on the mineral surface (Fig.6). The mineral material adsorbed with high concentration of Sb(V) did not obtain the characteristic peak of Sb<sub>2</sub>O<sub>5</sub> (Fig.7), indicating that there was no obvious deposition of Sb(V). After the deposition of Sb(III), it might exist in the form of Sb<sub>2</sub>O<sub>3</sub>, and Raman detection results showed obvious Sb<sub>2</sub>O<sub>3</sub> characteristic peaks. The Raman peaks at 190 and 452cm<sup>-1</sup> can be attributed to the bending vibration between Sb—O—Sb, while the Raman peaks at 256, 357, 374, and 715cm<sup>-1</sup> can be attributed to the stretching vibration between Sb—O—Sb (Fig.8). Raman spectroscopy can be used as a convenient method to monitor the adsorption and deposition of antimony on minerals.

## 参考文献

- [1] Babushok V I, Deglmann P, Krämer R, et al. Influence of antimony-halogen additives on flame propagation[J]. *Combustion Science and Technology*, 2017, 189(2): 290–311.
- [2] Nishad P A, Bhaskarapillai A. Antimony, a pollutant of emerging concern: A review on industrial sources and remediation technologies[J]. *Chemosphere*, 2021, 277: 130252.
- [3] Jia X, Ma L, Liu J, et al. Reduction of antimony mobility from Sb-rich smelting slag by Shewanella oneidensis: Integrated biosorption and precipitation[J]. *Journal of Hazardous Materials*, 2022, 426: 127385.
- [4] Li J, Zheng B H, He Y, et al. Antimony contamination, consequences and removal techniques: A review[J]. *Ecotoxicology and Environmental Safety*, 2018, 156: 125–134.
- [5] Filella M, Belzile N, Chen Y W. Antimony in the environment: A review focused on natural waters: I. Occurrence[J]. *Earth-Science Reviews*, 2002, 57(1–2): 125–176.
- [6] He M, Wang X, Wu F, et al. Antimony pollution in China[J]. *Science of the Total Environment*, 2012, 421: 41–50.
- [7] 牛斯达, 赵立群, 牛向龙, 等. 应用电子探针技术研究

- 桂西南下雷锰矿床锰钾矿的结构特征[J]. 岩矿测试, 2022, 41(2): 239–250.
- Niu S D, Zhao L Q, Niu X L, et al. The application of EPMA in the textural characterization of cryptomelane in the Xialei manganese deposit, Southwest Guangxi[J]. *Rock and Mineral Analysis*, 2022, 41(2): 239–250.
- [8] Dupont D, Arnout S, Jones P T, et al. Antimony recovery from end-of-life products and industrial process residues: A critical review[J]. *Journal of Sustainable Metallurgy*, 2016, 2(1): 79–103.
- [9] Chen L, Ren B, Deng X, et al. Potential toxic heavy metals in village rainwater runoff of antimony mining area, China: Distribution, pollution sources, and risk assessment[J]. *Science of the Total Environment*, 2024(920): 170702.
- [10] 孟郁苗, 胡瑞忠, 高剑峰, 等. 锡的地球化学行为以及锡同位素研究进展[J]. 岩矿测试, 2016, 35(4): 339–348.
- Meng Y M, Hu R Z, Gao J F, et al. Research progress on Sb geochemistry and Sb isotopes[J]. *Rock and Mineral Analysis*, 2016, 35(4): 339–348.
- [11] Su X, Wang X, Zhou Z, et al. Can antimony contamination in soil undermine the ecological contributions of earthworms?[J]. *Science of the Total Environment*, 2023, 904: 166305.
- [12] Vidya C S N, Shetty R, Vaculíková M, et al. Antimony toxicity in soils and plants, and mechanisms of its alleviation[J]. *Environmental and Experimental Botany*, 2022, 202: 104996.
- [13] Herath I, Vithanage M, Bundschuh J. Antimony as a global dilemma: Geochemistry, mobility, fate and transport[J]. *Environmental Pollution*, 2017, 223: 545–559.
- [14] Caplette J N, Wilson S C, Mestrot A. Antimony release and volatilization from organic-rich and iron-rich submerged soils[J]. *Journal of Hazardous Materials*, 2024, 470: 134230.
- [15] Chen L, Han Y, Li W, et al. Removal of Sb(V) from wastewater via siliceous ferrihydrite: Interactions among ferrihydrite, coprecipitated Si, and adsorbed Sb(V)[J]. *Chemosphere*, 2022, 291: 133043.
- [16] Kumar R, Jing C, Yan L. A critical review on arsenic and antimony adsorption and transformation on mineral facets[J/OL]. *Journal of Environmental Sciences* (2024-02-01). <https://doi.org/10.1016/j.jes.2024.01.016>
- [17] Zhou W, Zhou J, Feng X, et al. Antimony isotope fractionation revealed from EXAFS during adsorption on Fe(oxyhydr) oxides[J]. *Environmental Science & Technology*, 2023, 57(25): 9353–9361.
- [18] Hei E, He M, Zhang E, et al. Risk assessment of antimony-arsenic contaminated soil remediated using zero-valent iron at different pH values combined with freeze-thaw cycles[J]. *Environmental Monitoring and Assessment*, 2024, 196(5): 1–17.
- [19] Peng L, Wang N, Xiao T, et al. A critical review on adsorptive removal of antimony from waters: Adsorbent species, interface behavior and interaction mechanism[J]. *Chemosphere*, 2023: 138529.
- [20] Sun Q, Liu C, Alves M E, et al. The oxidation and sorption mechanism of Sb on  $\delta$ -MnO<sub>2</sub>[J]. *Chemical Engineering Journal*, 2018, 342: 429–437.
- [21] Nie J, Yao Z, Shao P, et al. Revisiting the adsorption of antimony on manganese dioxide: The overlooked dissolution of manganese[J]. *Chemical Engineering Journal*, 2022, 429: 132468.
- [22] Wu Y, Sun G, Huang J H, et al. Antimony isotopic fractionation during intensive chemical weathering of basalt in the tropics[J]. *Geochimica et Cosmochimica Acta*, 2024, 367: 29–40.
- [23] Zhou W, Zhou A, Wen B, et al. Antimony isotope fractionation during adsorption on aluminum oxides[J]. *Journal of Hazardous Materials*, 2022, 429: 128317.
- [24] Xi J, He M, Lin C. Adsorption of antimony(III) and antimony(V) on bentonite: Kinetics, thermodynamics and anion competition[J]. *Microchemical Journal*, 2011, 97(1): 85–91.
- [25] Dousova B, Lhotka M, Filip J, et al. Removal of arsenate and antimonate by acid-treated Fe-rich clays[J]. *Journal of Hazardous Materials*, 2018, 357: 440–448.
- [26] Zhang Y, Ding C, Gong D, et al. A review of the environmental chemical behavior, detection and treatment of antimony[J]. *Environmental Technology & Innovation*, 2021, 24: 102026.
- [27] Tang H, Hassan M U, Nawaz M, et al. A review on sources of soil antimony pollution and recent progress on remediation of antimony polluted soils[J]. *Ecotoxicology and Environmental Safety*, 2023, 266: 115583.
- [28] Schwertmann U, Cornell R M. Iron oxides in the laboratory: Preparation and characterization[M]. John Wiley & Sons, 2008.
- [29] Balboni E, Smith K F, Moreau L M, et al. Transformation of ferrihydrite to goethite and the fate of plutonium[J]. *ACS Earth and Space Chemistry*, 2020, 4(11): 1993–2006.
- [30] 崔婷, 叶欣, 朱霞萍, 等. 土壤铁锰氧化物形态测定及

- 吸附 Sb(Ⅲ) 的主控因子研究 [J]. *岩矿测试*, 2023, 42(1): 167–176.
- Cui T, Ye X, Zhu X P, et al. Determination of various forms of iron and manganese oxides and the main controlling factors of absorption of Sb(Ⅲ) in soil [J]. *Rock and Mineral Analysis*, 2023, 42(1): 167–176.
- [31] Wang X, He M, Lin C, et al. Antimony(Ⅲ) oxidation and antimony(V) adsorption reactions on synthetic manganite [J]. *Geochemistry*, 2012, 72: 41–47.
- [32] Sukul P, Lamshöft M, Zühlke S, et al. Sorption and desorption of sulfadiazine in soil and soil-manure systems [J]. *Chemosphere*, 2008, 73(8): 1344–1350.
- [33] Wu T, Liu C, Cui P, et al. Kinetics of coupled sorption and abiotic oxidation of antimony(Ⅲ) in soils [J]. *Geoderma*, 2023, 434: 116486.
- [34] Liu X, Wang Y, Xiang H, et al. Unveiling the crucial role of iron mineral phase transformation in antimony(V) elimination from natural water [J]. *Eco-Environment & Health*, 2023, 2(3): 176–83.
- [35] Mukhopadhyay R, Sarkar B, Barman A, et al. Arsenic adsorption on modified clay minerals in contaminated soil and water: Impact of pH and competitive anions [J]. *Clean-Soil, Air, Water*, 2021, 49(4): 2000259.
- [36] Li Y, Liu J, Wang Y, et al. Contribution of components in natural soil to Cd and Pb competitive adsorption: Semi-quantitative to quantitative analysis [J]. *Journal of Hazardous Materials*, 2023, 441: 129883.
- [37] Yan L, Chan T, Jing C. Mechanistic study for antimony adsorption and precipitation on hematite facets [J]. *Environmental Science & Technology*, 2022, 56(5): 3138–3146.
- [38] 随志磊. 极端条件下几种稀土盐和氧化锑的相变和发光研究 [D]. 合肥: 中国科学技术大学, 2017: 10–50.  
Sui Z L. Studies on phase transitions and photoluminescence of several rare earth sands and antimony trioxide in extreme conditions [D]. Hefei: University of Science and Technology of China, 2017: 10–50.
- [39] Pereira A L J, Gracia L, Santamaría-Pérez D, et al. Structural and vibrational study of cubic Sb<sub>2</sub>O<sub>3</sub> under high pressure [J]. *Physical Review B*, 2012, 85(17): 174108.
- [40] Abrashev M V, Ivanov V G, Stefanov B S, et al. Raman spectroscopy of alpha-FeOOH (goethite) near antiferromagnetic to paramagnetic phase transition [J]. *Journal of Applied Physics*, 2020, 127(20): 205108.
- [41] de Faria D L A, Lopes F N. Heated goethite and natural hematite: Can Raman spectroscopy be used to differentiate them? [J]. *Vibrational Spectroscopy*, 2007, 45(2): 117–121.
- [42] Chistyakova N, Antonova A, Elizarov I, et al. Mössbauer, nuclear forward scattering, and Raman spectroscopic approaches in the investigation of bioinduced transformations of mixed-valence antimony oxide [J]. *The Journal of Physical Chemistry A*, 2021, 125(1): 139–145.
- [43] Frost R L, Bahfenne S. Raman spectroscopic study of the antimonate mineral brizziite NaSbO<sub>3</sub> [J]. *Radiation Effects and Defects in Solids*, 2010, 165(3): 206–210.
- [44] Zahn D R T. Vibrational spectroscopy of bulk and supported manganese oxides [J]. *Physical Chemistry Chemical Physics*, 1999, 1(1): 185–190.
- [45] Julien C, Massot M, Rangan S, et al. Study of structural defects in  $\gamma$ -MnO<sub>2</sub> by Raman spectroscopy [J]. *Journal of Raman Spectroscopy*, 2002, 33(4): 223–228.
- [46] Shim S H, Duffy T S. Raman spectroscopy of Fe<sub>2</sub>O<sub>3</sub> to 62GPa [J]. *American Mineralogist*, 2002, 87(2–3): 318–326.
- [47] Marshall C P, Dufresne W J B. Resonance Raman and polarized Raman scattering of single-crystal hematite [J]. *Journal of Raman Spectroscopy*, 2022, 53(5): 947–955.
- [48] Basu A, Mookherjee M, Clapp S, et al. High-pressure Raman scattering and X-ray diffraction study of kaolinite, Al<sub>2</sub>Si<sub>2</sub>O<sub>5</sub>(OH)<sub>4</sub> [J]. *Applied Clay Science*, 2023, 245: 107144.
- [49] Frost R L, Fredericks P M, Kloprogge J T, et al. Raman spectroscopy of kaolinites using different excitation wavelengths [J]. *Journal of Raman Spectroscopy*, 2001, 32(8): 657–663.
- [50] Delbé K, de Sousa C, Grizet F, et al. Determination of the pressure dependence of Raman mode for an alumina-glass pair in hertzian contact [J]. *Materials*, 2022, 15(23): 8645.
- [51] Misra A, Bist H D, Navati M S, et al. Thin film of aluminum oxide through pulsed laser deposition: A micro-Raman study [J]. *Materials Science and Engineering B*, 2001, 79(1): 49–54.